

See discussions, stats, and author profiles for this publication at: <https://www.researchgate.net/publication/231371181>

Simulation of Unsteady Flow and Vortex Shedding for Narrow Spacer-Filled Channels

ARTICLE *in* INDUSTRIAL & ENGINEERING CHEMISTRY RESEARCH · AUGUST 2003

Impact Factor: 2.59 · DOI: 10.1021/ie030211n

CITATIONS

47

READS

45

3 AUTHORS, INCLUDING:



Dianne Wiley

University of New South Wales

152 PUBLICATIONS **2,792** CITATIONS

SEE PROFILE



David Frederick Fletcher

University of Sydney

279 PUBLICATIONS **5,125** CITATIONS

SEE PROFILE

Unsteady Flows with Mass Transfer in Narrow Zigzag Spacer-Filled Channels: A Numerical Study

G. A. Fimbres-Weihs,[†] D. E. Wiley,^{*,†} and D. F. Fletcher[‡]

School of Chemical Engineering and Industrial Chemistry, UNESCO Centre for Membrane Science and Technology, University of New South Wales, Sydney, NSW 2052, Australia, and Department of Chemical Engineering, The University of Sydney, Sydney, NSW 2006, Australia

A computational fluid dynamics (CFD) model was used to simulate unsteady fluid flow with mass transfer in two-dimensional narrow channels containing zigzag spacers. A solute with a Schmidt number of 600 dissolving from the wall and channel Reynolds numbers up to 1683 were considered. Time averaging and Fourier analysis were performed to gain insight into the dynamics of the different flow regimes encountered, ranging from steady flow to vortex shedding behind the spacer filaments. The relationship between vortex shedding, pressure drop, and mass-transfer enhancement was explored. It was found that, at a Reynolds number between 526 and 841, the flow becomes unsteady. As the Reynolds number increases, the region of maximum mass transfer moves upstream from the wall opposite the downstream spacer to the region between spacers. The regions of high mass transfer are correlated not only to those of high shear rate but also to those where the fluid flow is toward the wall. Two main causes for mass-transfer enhancement were found: increased wall shear and an inflow of lower concentration fluid into the boundary layer, with the latter dominating unsteady mass-transfer enhancement for membrane filtration of sodium chloride.

1. Introduction

Since the work of Loeb and Sourirajan¹ in the late 1950s, membrane processes have evolved to become cost-effective industrial separation techniques. Reverse osmosis (RO), nanofiltration (NF), ultrafiltration (UF), and microfiltration (MF) are considered among the best available technologies for water treatment. Hollow fiber and spiral wound membrane (SWM) modules are the most common commercially available membrane modules. The latter dominate, especially for RO and NF, and are the focus of this study. The main difficulty these types of modules face is the development of a high-concentration layer near the membrane surface, an effect referred to as “concentration polarization”. Apart from reducing the flux of solvent through the membrane, concentration polarization also accelerates the onset of fouling.

Concentration polarization arises because of the convective transport of solutes from the bulk and their rejection at the membrane surface being faster than the diffusive transport back to the bulk. The effect of concentration polarization in SWM modules is reduced by the spacer nets also used to keep the membrane leaves apart. It has been shown, both experimentally² and numerically,³ that the presence of spacers in narrow channels promotes flow instabilities and increases mixing. Schock and Miquel⁴ analyzed experimentally several types of commercial spacers for their pressure drop and mass-transfer characteristics and developed correlations for the friction factor and the mass-transfer coefficient. In laminar flow, they calculated an exponent of 0.33 for the Reynolds number dependence of the Sherwood number in an empty channel and an exponent of 0.875 for this dependence in a spacer-filled channel. They also found that, in the turbulent regime, the exponent for the Reynolds number dependency in the spacer-filled channel did not vary from the value obtained for the laminar regime.

Kang and Chang⁵ obtained steady-state numerical solutions for flow and mass transfer in a two-dimensional narrow channel with rectangular turbulence promoters of the zigzag and cavity types. They solved the vorticity-stream function formulation of the Navier–Stokes equations using periodic boundary conditions and validated their results by flow visualization. They concluded that the flow becomes unsteady at a channel Reynolds number between 250 and 300, which translates to a hydraulic Reynolds number between 455 and 545.

Da Costa et al.⁶ developed a correlation for calculating the pressure drop of a spacer-filled channel, taking into account viscous and form drag on the spacer surface, viscous friction on the channel walls, and kinetic energy losses due to directional flow change. This correlation uses spacer characteristics such as mesh size and angle and, therefore, can be used in designing netlike spacers. They also performed flow visualization experiments using air bubbles and dye, where they observed that, at lower Reynolds numbers, the bulk of the flow follows a zigzag path.

As a recent review paper by Ghidossi et al.⁷ points out, computational fluid dynamics (CFD) has become a more widely used tool in the field of membrane science, with more and more research groups opting for this technique in order to gain insight into the phenomena taking place inside membrane modules and to assist the design processes and improve the performance of these modules. Particular emphasis has been put on the simulation of spacer-filled channels both in two dimensions^{2,8–15} and three dimensions,^{16–18} although few^{14,17} have ventured into the realm of transient flow. Particle image velocimetry (PIV) is an experimental technique also used for analyzing fluid flow and has been recently applied to membrane applications with encouraging results.¹⁹ However, improvements are required in order to obtain accurate time-dependent measurements.

Schwinge et al.^{2,8,9} used a commercial CFD package (CFX4) to perform steady-state, two-dimensional numerical simulations with and without mass transfer, as well as transient simulations, but only without mass transfer. Submerged, cavity, and zigzag cylindrical spacer configurations in a SWM module were

* Corresponding author. Tel.: +61 2 9385 5541. E-mail: d.wiley@unsw.edu.au.

[†] The University of New South Wales.

[‡] The University of Sydney.

examined. They varied the distance between spacers and the diameter of the filaments. The characteristics of the flow for each of the geometries were studied at different Reynolds numbers, emphasizing their impact on pressure drop, wall shear, and mass transfer.

Similar work was carried out by Gerald et al.,^{10,11} who performed steady-state, two-dimensional laminar simulations of the flow in a slit. However, their model included a semipermeable wall as one of the boundaries, unlike the dissolving wall employed by Schwinge et al.,⁸ and covered a range of Schmidt numbers from 570 to 3200. Although they employed experimental values for their permeate flux, they used a model which assumes diffusional transport through the membrane to predict its intrinsic rejection coefficient. They found the hydrodynamic boundary layer thickness to be insensitive to the permeation velocity, but found the concentration boundary layer thickness to be strongly correlated with the permeation velocity. They also performed simulations with the same parameters but in a channel filled with over 50 square filaments.^{12,13} They came to the important conclusion that the disruption of the concentration boundary layer has a strong effect on the concentration polarization distribution along the channel, and therefore, placing spacer filaments adjacent to both channel walls enhances mass transfer.

Using a three-dimensional spatially periodic CFD model, Li et al.¹⁸ found an optimal geometry for nonwoven spacers at $l_m/h_{ch} = 4$, which maximizes the Sherwood number while keeping energy losses due to pressure drop low. Their calculations included the mass transfer of a solute with Schmidt number of 1278, and their channel Reynolds numbers varied from 100 to 500 (hydraulic Reynolds number from 441 to 2205). They found that, in the geometries they analyzed, vortex shedding occurred for channel Reynolds numbers >150 , or hydraulic Reynolds numbers >662 .

Karode and Kumar¹⁶ carried out steady-state, three-dimensional simulations of laminar fluid flow without mass transfer in a test cell filled with nonwoven net type spacers. The spacers were simulated as cylindrical rods, whose geometric characteristics (diameter, angle, etc.) were taken from commercially available spacers for membrane modules. They modeled the whole test cell with a flat velocity profile at the cell entrance and constant pressure at the outlet. Depending on the characteristics of the spacers, between 8 and 12 filaments were placed in the flow domain. They concluded that a higher degree of mixing in the bulk does not necessarily translate to higher shear at the membrane walls. Their simulations showed a similar zigzag path of the bulk of the fluid to the one observed experimentally by Da Costa et al.,⁶ but only for spacers with large interfilament distance-to-filament diameter ratios. However, for spacers with low interfilament distance-to-filament diameter ratio, they noticed that the bulk of the fluid flows parallel to the spacer filaments, changing direction only when the flow reaches the lateral walls of the test cell. In this latter case, they found that most of the pressure drop across the channel was due to the shear between the top and bottom layers of fluid moving in different directions. In more recent work, Ranade and Kumar¹⁷ used a periodic "unit cell" approach to model rectangular and curvilinear three-dimensional spacer-filled channels and found that curvature did not influence fluid behavior significantly, unlike the shape of the spacer filaments. Although they also included mass-transfer effects in their calculations, it is unclear how they coupled this to the periodic boundary condition of their unit cell, in particular for their transient simulations.

Also using periodic boundary conditions, Koutsou et al.¹⁴ employed a commercial CFD code (FLUENT, v. 6.0.12) to simulate unsteady two-dimensional fluid flow without mass transfer around an array of submerged cylindrical spacers. They examined the effect of Reynolds number on pressure drop and wall shear and found that, for cylinder Reynolds numbers >60 (hydraulic Reynolds number >190), the flow becomes time-dependent, destabilized through a Hopf bifurcation. For Reynolds numbers higher than, but in the vicinity of, this bifurcation, the flow becomes periodic in time, with an increasing degree of chaos as the flow increases above the destabilization point. This was corroborated by the frequency spectra of the flow oscillations, which showed the appearance of more harmonics as the Reynolds number increases. They also identified that the dominant frequency corresponds to the Strouhal number, the dimensionless shedding frequency.

Despite the numerous CFD studies of the behavior of fluid flow in spacer-filled channels, the transient nature of mass-transfer enhancement in unsteady flow, especially in the near-wall region, is not yet fully understood. Given that membrane modules operate in a flow regime where unsteady flow may be present, it is important to understand the effect of transient flow. This work aims to use CFD to simulate and allow the analysis of the dynamics of fluid flow and mass transfer in narrow, spacer-filled channels such as those encountered in SWM modules. The effect of the Reynolds number on the flow regime and mass transfer will also be assessed. This work extends that of Schwinge et al.,² who studied two-dimensional unsteady flow without mass transfer and steady flow with mass transfer. In the latter type of flow, the high concentration gradients in the near-wall region require a large number of grid nodes to achieve suitable convergence of the mass-transport equation in that region. We, therefore, focus this paper on a two-dimensional case as an approximation to more complex geometries. Moreover, a dissolving-wall approach to mass transfer is utilized, following the work of Schwinge et al.⁸ for steady-state flows with mass transfer. Such an approach not only provides insights into the fluid behavior inside real modules but also allows us to establish some baseline conditions in order to develop a suitable approach to three-dimensional modeling.

2. Problem Description, Assumptions, and Methods

For this work, a commercial CFD code (ANSYS CFX-10.0) is used to solve the continuity, momentum, and mass-transport equations²⁰ in a spacer-filled channel. Previous work^{21,22} has shown that neither gravity nor density variation will have a significant effect on the solutions obtained; therefore, constant properties are employed and the effect of gravity is excluded. To further simplify this system, the fluid is assumed to be Newtonian, the flow is assumed to be two-dimensional, and only a binary mixture of water and salt is considered, with no sources of salt in the fluid. Moreover, mass transfer is incorporated in the form of a dissolving-wall boundary condition. Although a more accurate boundary condition for real-life membrane applications would be a permeable wall,^{15,22} the dissolving wall approximation is still capable of providing valuable insights into the transient mass-transfer phenomena taking place within the boundary layer, without adding complexity to an already large computational problem.

Schwinge et al.² indicate that large computational times (between 50 and 150 h on a NEC SX5 supercomputer) and memory (>2 GB) were required for each simulation with no mass transfer. When mass transfer is included, even larger convergence times would be anticipated, since an additional

3.1. Steady Flow. For the simulations up to a Reynolds number of 526, the flow was steady, with no variation of the flow variables at any point in the channel as time progressed. For these steady simulations, the calculated flow was the same as that described by Schwinge et al.,⁹ where the zigzag pattern of the spacers forces the flow to follow that same pattern. Small recirculation regions were observed upstream of each filament, and larger recirculation regions were located downstream of each filament. At a Reynolds number of 526, as seen in Figure 2, the larger recirculation region reattaches to the membrane wall just upstream of the next filament. As noted by Schwinge et

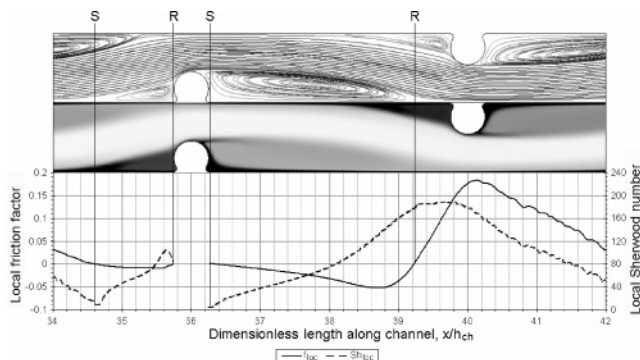


Figure 2. Streamline (top), salt concentration (middle), local friction factor, and Sherwood number plots along the bottom channel wall at a Reynolds number of 526, showing separation (S) and reattachment (R) points.

al.,⁸ concentration was higher within the recirculation regions than in the bulk flow because of the flow recirculation. Development of the concentration boundary layer was disturbed by the higher shear caused by the reduction of the channel cross section due to the filament on the opposite wall.

As seen in Figure 2, the maximum local Sherwood number along the membrane wall is located near the point of reattachment of the larger recirculation region, and the minima are located at the separation point of both recirculation regions. Since mass transfer at the membrane wall is directly proportional to the local Sherwood number, these are also the points of maximum and minimum mass transfer, respectively. This suggests that separation points are associated with regions of low mass transfer, as are reattachment points with regions of high mass transfer.

At a point of reattachment, there is flow of low-concentration fluid toward the channel wall, where a high salt concentration is located. At the same time, flow within the boundary layer is away from the point on reattachment. These two combine to create a low salt concentration and, therefore, a high salt concentration gradient at the point of reattachment. Likewise, at a point of separation, the high concentration at the membrane wall means there is convection of high-concentration fluid along the boundary layer toward that point and then away from the wall, toward the bulk. Therefore, a high salt concentration region is formed at the reattachment point, which in turn slows diffusion from the wall.

The boundary layer can be thought of as a layer of fluid near the boundary in which only molecular transport is taking place on the plane perpendicular to this layer, and transport due to convection in this direction is negligible.²⁶ Using this definition, the velocity and concentration boundary layers can be calculated, respectively, by

$$\delta_{vel} = \frac{u_{eff}}{\text{abs}\left(\frac{\partial u}{\partial y}\right)_w} \quad (1)$$

$$\delta_{conc} = \frac{Y_b - Y_w}{\left(\frac{\partial Y}{\partial y}\right)_w} \quad (2)$$

The dimensionless boundary layer thicknesses along the bottom channel wall can be seen in Figure 3. Comparing Figures 2 and 3, it can be seen that the regions of high shear rate correspond to regions where the developing concentration boundary layer is thinner. In particular, the shear rate maxima are located at the points on the channel wall opposite the filaments. From eq 1, it can also be seen that the velocity

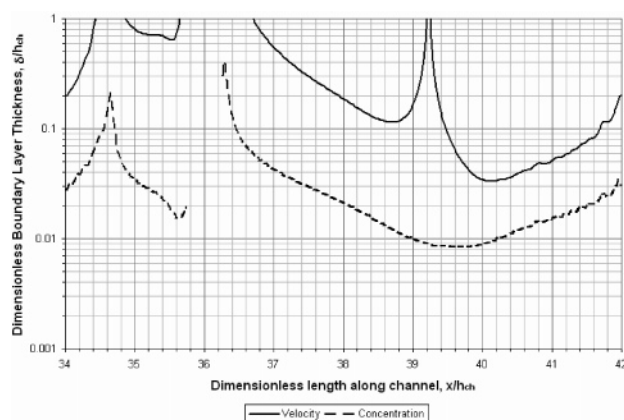


Figure 3. Dimensionless concentration and velocity boundary layer thickness along the bottom channel wall at a Reynolds number of 526. The thicknesses were calculated using eqs 1 and 2.



Figure 4. Paths followed by the "eye" of shed vortices at Reynolds number 841 for the fourth unit cell of the computational domain.

boundary layer thickness is inversely proportional to the wall shear rate. Moreover, a thinner velocity boundary layer allows the lower concentration bulk flow to come closer to the wall. Given that the shear maxima are located just downstream of the reattachment point, this reasoning explains why the region of high mass transfer is shifted slightly downstream of the reattachment point, where the velocity boundary layer is thinner.

3.2. Moderately Unsteady Flow. At a Reynolds number of 841, the flow is unsteady. Vortices form behind each filament and at the membrane walls and move downstream with the bulk flow. As opposed to the case at lower Reynolds numbers where the flow was steady and there were only two recirculation regions located around each spacer (a smaller one upstream and a larger one downstream), at this Reynolds number there can be as many as three vortices between successive filaments at any one time, both upstream and downstream of each spacer along the membrane wall.

Figure 4 depicts the paths that the "eyes" of the shed vortices take through the channel. These paths were recorded over a period of ~ 0.6 s. It can be seen that there are mainly two locations where vortices are formed: behind a spacer and at the wall approximately two-thirds of the way between successive spacers. Two vortices with opposite rotation form behind each filament; however, the vortex that is formed closer to the wall is smaller in size than the one near the center of the channel, and the former usually decays or is forced against the wall by the latter. It should also be pointed out that, although the paths followed by eddies closer to the center of the channel are similar, they all differ slightly. This last observation is evidence that the flow has been through more than one bifurcation, as it has lost its time periodicity.

Figure 5 shows snapshots of the velocity vectors in the channel at successive time steps 6.1 ms apart and numerically identifies the shed vortices. As opposed to Figure 4, Figure 5 shows the position of the vortices relative to each other at different time steps. The smaller vortices are not labeled in Figure 5, because the velocity of the circulating fluid is too small compared with the larger vortices and cannot be distinguished in a vector plot of the scale used.

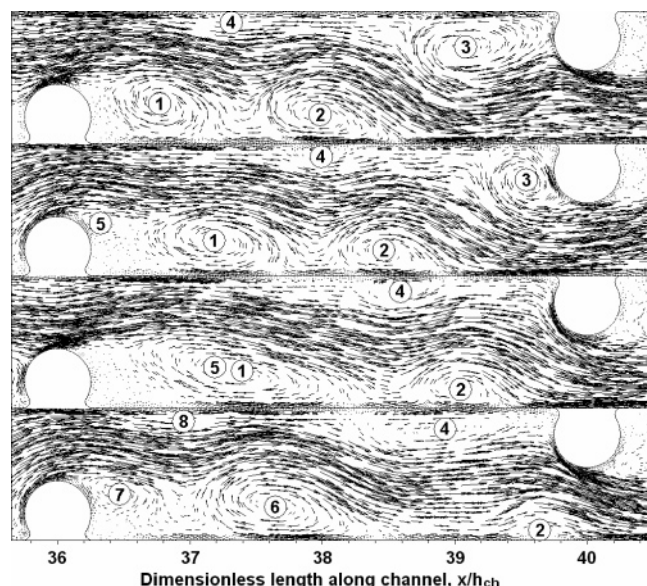


Figure 5. Velocity vector plots at a Reynolds number of 841 showing the 7th and 8th filaments from the channel inlet. Successive images are 6.1 ms apart. Shed vortices are identified by numbers 1–8.

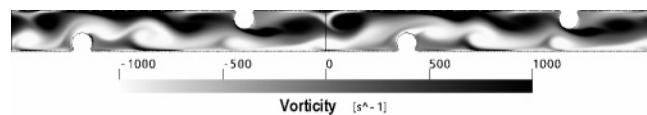


Figure 6. Snapshot of the vorticity contour plot at a Reynolds number of 841 showing the 7th–10th filaments from the channel inlet.

The shedding pattern shown in Figure 5 is similar to the one described by Schwinge et al.² for this spacer configuration. Vortices are formed at approximately regular intervals behind the spacer filaments (~ 12.2 ms) and at the membrane walls (~ 24.4 ms). It is interesting to notice how successive shed vortices behind the upstream spacer “merge” or “coalesce” before continuing downstream, as is evidenced by vortices 1 and 5, as depicted in Figure 5. However, such coalescence is not observed for every pair of eddies, and although the vortex shedding is quite regular and follows similar patterns, no two vortices follow the exact same path, as evidenced by Figure 4.

Because of the fact that the larger vortices near the bottom wall always rotate clockwise, and the ones near the top wall rotate counterclockwise, the wall shear resulting from the larger vortices scouring the channel walls is always of opposite sign to that resulting from the bulk flow.

As they move downstream, all vortices take on an elliptical shape and grow in size. They grow to approximately half of the channel height, until they reach half of the way to the downstream filament. After that, the size of the vortices decreases until they are ultimately squeezed between the downstream filament and the membrane wall. At that point, they disappear momentarily only to later reappear downstream. This squeezing phenomenon can be clearly observed in Figure 6, which shows how the vorticity contours are squeezed between each filament and the opposite wall.

As the vortices move downstream, Figure 7 shows how they move high-concentration fluid from the near-wall region to the bulk of the fluid and low-concentration fluid from the bulk to the wall. They also mix the low- and high-concentration fluids in a rotating motion. When a vortex scours the channel wall, the salt from the near-wall region is first carried upstream and then moves toward the center of the channel following the rotation of the eddy carrying it.

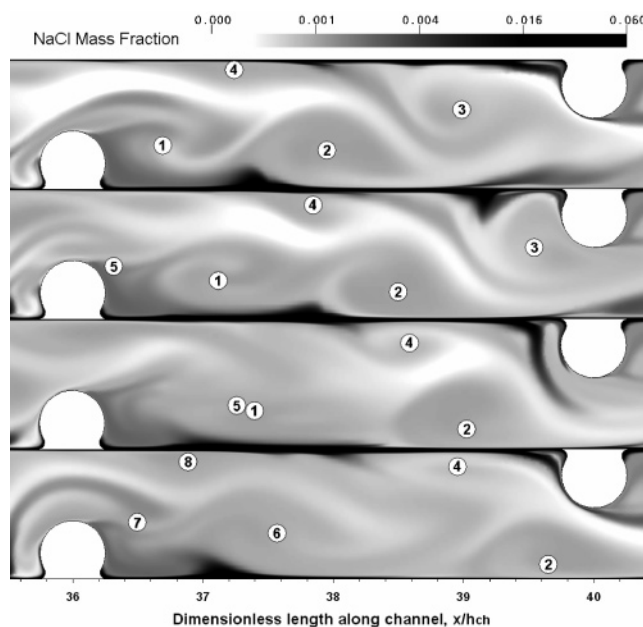


Figure 7. Evolution of salt concentration at a Reynolds number 841. Successive images are 6.1 ms apart and correspond to the times and filaments shown in Figure 5. Shed vortices are identified by numbers 1–8.

A region of high relative salt concentration can be observed behind the upstream filament in Figure 7. By comparison with the vector plot (Figure 5), this is also a region of low velocity or stagnant fluid. Therefore, the salt concentration builds up at that point for the same reasons as in the steady flow cases at lower Reynolds numbers. As for the high concentration regions present in front of the filaments in steady flow, they are not present at this Reynolds number. As the counterclockwise eddies formed along the channel wall (number 3 in Figure 7) come closer to the upstream filament, they move lower-concentration fluid from the middle of the channel to the region in front of the filament and simultaneously eject high-concentration fluid from this region into the bulk flow.

The local Sherwood number and friction factor distribution along the bottom wall region between successive filaments is depicted in Figure 8. For reasons mentioned before, local negative friction factor minima indicate the position of a vortex near the channel wall. It can be seen that the maxima in local Sherwood number, identified by lines A–F in Figure 8, mostly correspond to the front of the vortex which is scouring the wall (eddy number 2 in Figures 5 and 7). This supports the earlier contention that high mass-transfer regions should be expected near the reattachment point of a recirculation region as, in that vicinity, low-concentration flow is being forced closer to the channel wall, thus increasing the concentration gradient. This relationship is loosely confirmed in Figure 8, except that the local Sherwood number maxima at a given instant are always slightly behind the reattachment points. This is understandable if one takes into account the fact that the time scales for momentum transfer are smaller than those for mass transfer for Schmidt numbers above 1, as evidenced by the lag in the local Sherwood number distribution when compared with the local friction factor at any point in time.

3.3. Highly Unsteady Flow. At a Reynolds number of 1683, the flow pattern is unsteady, as was the case at the Reynolds number of 841. Again, there is vortex shedding behind the spacer filaments and from the channel walls, and a maximum of three vortices can be found on opposite sides of each spacer filament. However, at this higher Reynolds number, the vortices found in the channel are visibly larger in size than those found

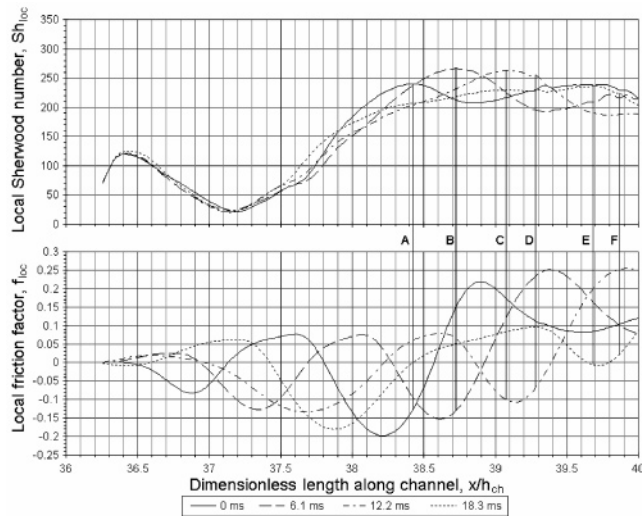


Figure 8. Local Sherwood number and friction factor along bottom channel wall at a Reynolds number of 841, corresponding to the times shown in Figure 5. Lines A, B, C, and E identify the maximum local Sherwood number at each time. Lines D and F identify local maxima of local Sherwood number for the last two times presented.

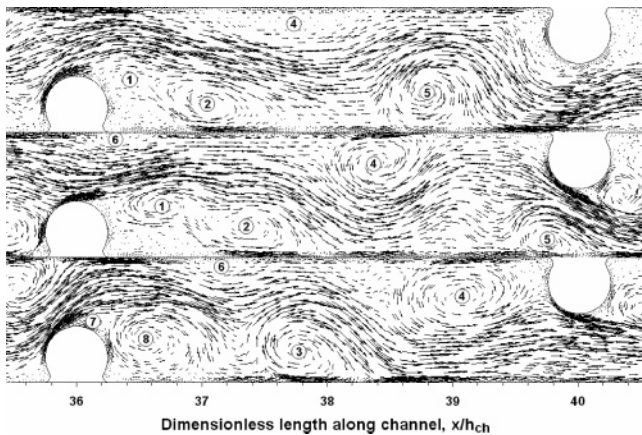


Figure 9. Velocity vector plots at a Reynolds number of 1683 showing the 7th and 8th filaments from the channel inlet. Successive images are 4.58 ms apart. Shed vortices are identified by numbers 1–8.

at the lower Reynolds number of 841, and as they flow downstream, they continue to grow in size until they are $\sim 90\%$ of the way to the downstream filament. Moreover, their shape is round rather than elliptical, and they usually occupy more than half of the channel height.

The vortex shedding pattern at this Reynolds number presents characteristics not found at the lower Reynolds number of 841, even though they are similar. At the higher Reynolds number, the eddy shedding pattern is not one per period, but rather two vortices shed successively within a short period (~ 2 ms), followed by a longer period (~ 5 ms) before the cycle repeats itself. After the first vortex is shed (see eddy number 2 in Figure 9), it remains relatively stationary for a few milliseconds, until the second vortex is shed (eddy number 1) and merges with the first. Subsequently, the newly formed vortex (eddy number 3) continues downstream. As opposed to the observed behavior at the lower Reynolds number, in this case, vortex merging occurs for every eddy pair. However, the merging pattern is by no means periodic in time. Some of the variations observed are as follows:

- a longer time between the first and second eddy shedding (~ 12 ms);

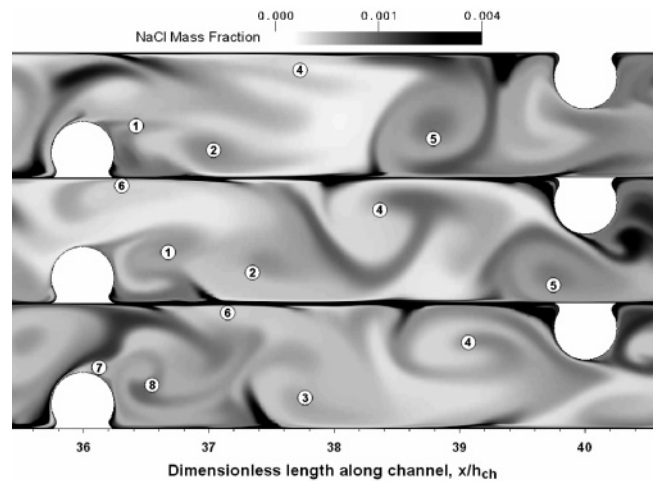


Figure 10. Evolution of salt concentration at Reynolds number 1683. Successive images are 4.58 ms apart and correspond to the times and filaments shown in Figure 9. Shed vortices are identified by numbers 1–8.

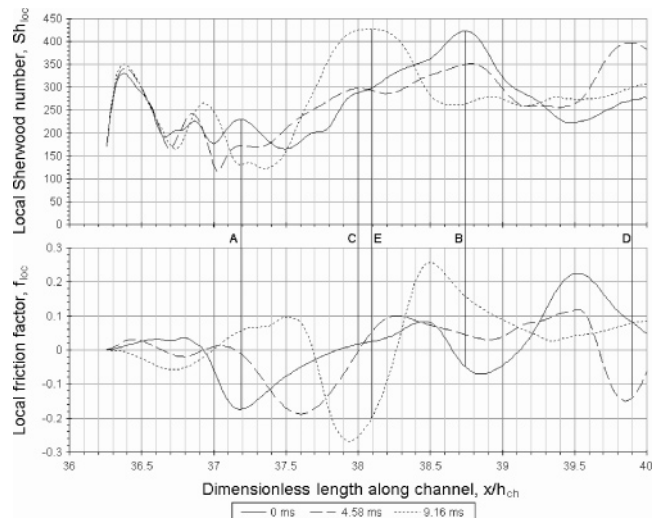


Figure 11. Local Sherwood number and friction factor along bottom channel wall at a Reynolds number of 841, corresponding to Figure 9. Lines A–E identify local maxima of the local Sherwood number associated with wall scouring vortices.

- the eddy resulting from the first merger remaining stationary until a third eddy joins it; and
- a third eddy catching up with the moving vortex that resulted from the first merger. These two vortices merge approximately halfway to the downstream spacer.

The mechanisms by which salt is convected from the near-wall region into the bulk flow are the same as for the lower Reynolds number cases. However, because of the larger size of the vortices at this Reynolds number, the high-concentration fluid ejected from one wall region can potentially reach the opposite channel wall and reduce the concentration gradient there, thus reducing the local Sherwood number. This phenomenon can be observed in Figure 10 for eddy numbers 4 and 5.

Figure 11 shows the local Sherwood number and friction factor profiles along the bottom channel wall. Lines A and C correspond to eddy number 2, line E corresponds to eddy number 3, and lines B and D correspond to eddy number 5. As was the case at a Reynolds number of 841, Sherwood number maxima can be associated with corresponding vortices scouring the wall and lagging slightly behind the reattachment point. However, at this Reynolds number, local Sherwood number maxima caused by passing eddies can be found before the

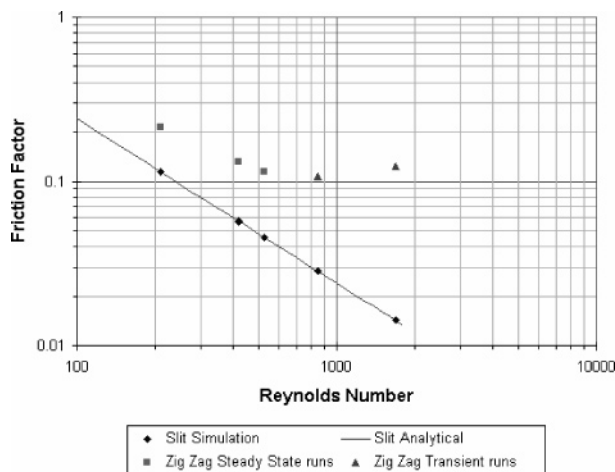


Figure 12. Friction factor dependency on Reynolds number.

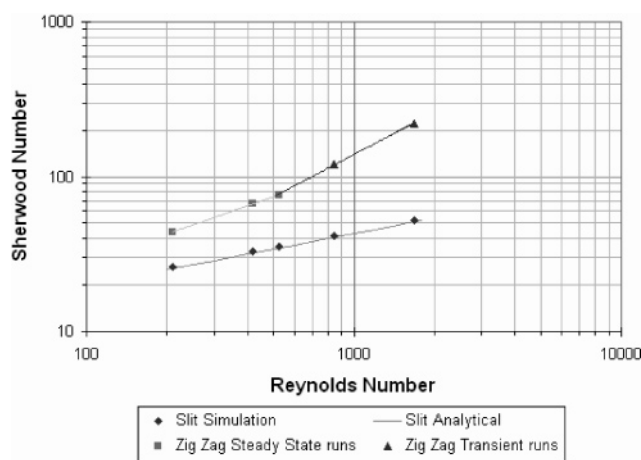


Figure 13. Sherwood number dependency on Reynolds number at a Schmidt number of 600.

halfway mark between successive spacer filaments (Line A), which was not the case in the flow with a Reynolds number of 841. Moreover, it can be observed that there is a local minimum just downstream of Line C at the 4.58 ms curve, which is caused by the high-concentration fluid moving toward the bottom wall due to eddy number 4.

3.4. Friction Factor and Sherwood Number. The average friction factor and Sherwood number for the spacer unit cell that comprises filaments numbers 7 and 8 were calculated for each of the runs, for both the channel with the zigzag spacer and an empty channel at the same distance downstream where the previously mentioned filaments would be located. The results obtained are summarized in Figures 12 and 13.

Figure 12 shows that, between Reynolds numbers of 841 and 1683, the friction factor increases, which indicates that the flow over that Reynolds number range is in the transition region between laminar and turbulent flow. This agrees with the results obtained by Schwinge et al.^{2,8} using a different CFD software package (CFX 4.3, AEA Technology) and a structured quadrilateral mesh, as opposed to the unstructured meshing approach used in this work. Their data also shows an increase in the friction factor as the Reynolds number goes from 800 to 1600.

Figure 13 shows that, as expected, the Sherwood number increased with increasing Reynolds number. Assuming a power law dependence of the Sherwood number with respect to the Reynolds number of the form²⁷

$$Sh = cRe^a Sc^b \left(\frac{d_h}{L}\right)^d \quad (3)$$

the exponent a for the Reynolds number dependence of the Sherwood number, for both the empty channel and the channel with the zigzag spacer, was calculated from the data shown in Figure 13. At steady state, the exponent was 0.332 for the empty channel and 0.605 for the zigzag spacer. Under unsteady flow conditions, the exponent increased to 0.92 for the zigzag spacer, which indicates that the higher degree of mixing caused by the vortices enhances mass transfer. These findings are similar to the experimental results of Schock and Miquel,⁴ who calculated a value for the Reynolds number exponent of 0.33 for the empty channel case and 0.875 for the spacer-filled channel case. They also agree with the results of Da Costa,²⁷ who found values for the exponent in the range of 0.40–0.60 for the laminar regime, using Reynolds numbers below 100.

3.5. Comparison of Velocity and Concentration Effects.

Monitoring points were placed at several locations on the top membrane wall of the spacer unit cell, in regions where the highest and lowest wall shear rates were expected, as well as at some other random points along the wall (see Figure 14). At these points, the salt concentration and velocity gradients were recorded for each of the runs. The data were used to calculate the root mean square (RMS) velocity and concentration boundary layer thickness at each wall monitoring point. The results of this calculation, given in Figure 15, show the correlation between the velocity (shear) and the concentration (mass transfer) boundary layer thicknesses. Although a correlation coefficient of 0.701 does not indicate a strong dependence, it does confirm that a thinner velocity boundary layer generally results in a thinner concentration boundary layer. Figure 15 also shows that the concentration boundary layer is ~1 order of magnitude smaller than its corresponding velocity boundary layer, which agrees with the predictions of Bird et al.²⁰

Velocity and mass fraction data were also collected every 100 time steps along the channel walls. Using this information, the RMS of the local friction factor as well as the Sherwood number profiles along the bottom channel wall for various Reynolds numbers were calculated and are depicted in Figures 16 and 17, respectively. Along the top wall, these profiles are approximately the same, only shifted 8 mm to the right. These graphs also show the range that these variables cover, which is represented by the shaded regions.

As the Reynolds number increases, the local friction factor maximum decreases and moves from being closer to the downstream spacer ($x/h_{ch} \approx 40$ at $Re = 210, 526$, and 841) toward the upstream filament ($x/h_{ch} \approx 37.8$ at $Re = 1683$). Moreover, in the laminar regime, there is zero friction at the location of the reattachment points, which leads to there being two distinct local maxima for the local friction factor. It can also be seen that the region in front of the upstream filament has higher friction in the unsteady cases than in the steady ones, which agrees with the general trends for friction factor.

The behavior of the local friction factor over the wall region opposite the downstream spacer is also different for Reynolds numbers 841 and 1683. In the former case, no vortices scour the wall in the region of $40 \leq x/h_{ch} \leq 41$, as evidenced by the fact that the local friction factor does not change sign in that section. However, at the higher Reynolds number, the whole of the channel wall experiences both positive and negative local friction factors, which means that eddies sweep the entire wall region at some time or another. It also means that a vortex shed upstream affects the shedding of vortices further downstream

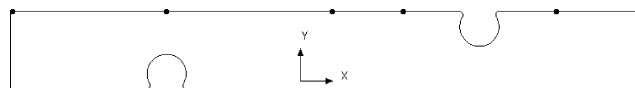


Figure 14. Location of the wall monitoring points in the spacer unit cell.

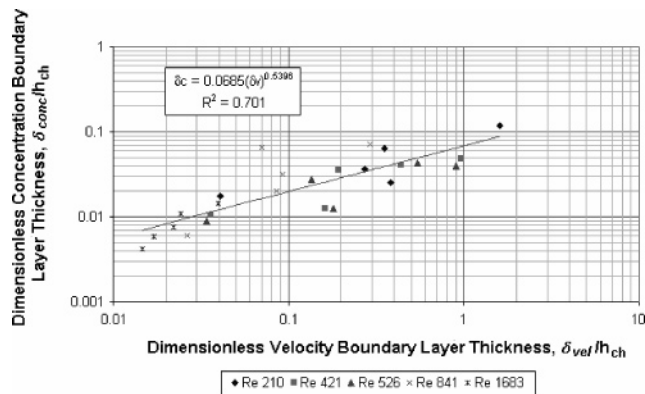


Figure 15. Correlation between friction factor and Sherwood number at the wall monitoring points shown in Figure 14.

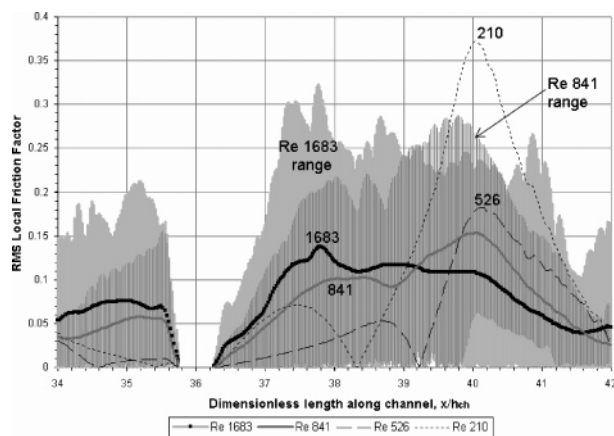


Figure 16. Friction factor distribution along bottom channel wall for the fourth unit cell of the computational domain. Shaded areas show the range of this variable for the transient runs.

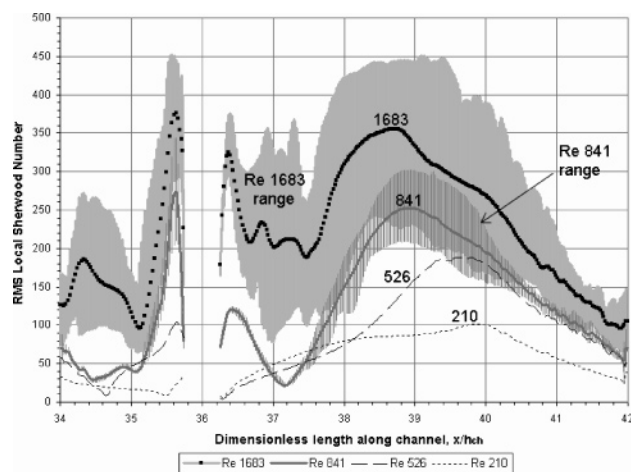


Figure 17. Local Sherwood number distribution along bottom channel wall for the fourth unit cell of the computational domain. Shaded areas show the range of this variable for the transient runs.

at a Reynolds number of 1683, but not at 841, since the eddy has already disappeared before it reaches the region where the next vortex is shed.

From Figure 17, it can be seen that, as the Reynolds number increases, the region of higher mass transfer moves upstream, from being closer to the downstream filament to the region

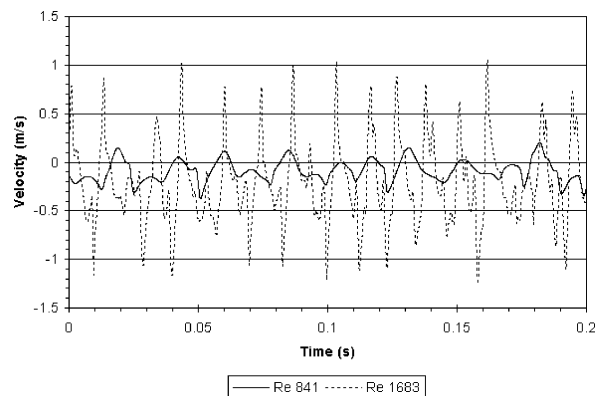


Figure 18. Time evolution of velocity in the y direction between successive spacers, at the middle of the channel.

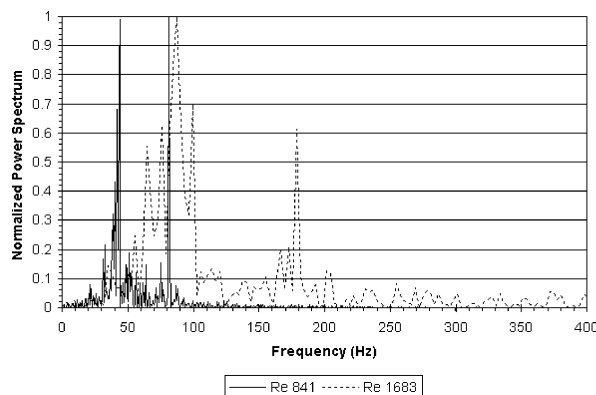


Figure 19. Power spectrum for velocity in the y direction between successive spacers, at the middle of the channel.

between the spacers. This corresponds with the upstream movement of the friction factor maximum. Moreover, a region of high mass transfer also appears near both sides of the filament as the Reynolds number increases. This latter phenomenon is caused by vortices renewing the high-concentration fluid with lower-concentration fluid as they come near the filaments.

3.6. Fourier Analysis. To obtain further information about the dynamics of the momentum and mass-transport processes in the membrane channel, a Fourier analysis was carried out. A monitoring point was placed in the middle of the channel ($y = (1/2)h_{ch}$) between successive spacers. Velocity and salt concentration were recorded at that point for each time step, the fast Fourier transform (FFT) was applied to this time data, and the frequency spectra were obtained by calculating the square of the absolute value of the FFT. However, only the velocity perpendicular to the bulk flow gave meaningful information about the flow. The time series for this variable can be seen in Figure 18.

Because of the monitoring point being placed halfway between successive spacers, it can be seen from Figures 5 and 9 that it is mainly the vortices shed by the upstream spacer that affect this point. For both unsteady cases, at Reynolds numbers of 841 and 1683, the flow was not periodic in time nor did it follow a time-repetitive vortex-shedding pattern. This agrees with observations made previously in relation to Figures 5 and 9. Moreover, at the higher Reynolds number, the oscillations have a larger amplitude and their frequency is also slightly higher.

From Figure 19, it can be seen that there are two main frequencies for both of the transient runs presented there. For the run at Reynolds number 841, the strongest peak is at a frequency of 81.5 Hz (period of 12.3 ms). There is a second

strong peak at 43.7 Hz (period of 22.9 ms), and frequencies in the range of 37 to 43.5 Hz also contribute significantly to the spectrum. The higher frequency corresponds to the vortex-shedding frequency, and the lower frequency corresponds to the frequency with which large eddies go past the monitoring point (see Figure 5). The latter also loosely correspond to the frequency with which local positive v velocity maxima appear in Figure 18.

The run at a Reynolds number of 1683 also presents two strong frequency regions. However, the lower-frequency region is broader at this Reynolds number than at the lower one. In this case, it covers the range from 60 to 100 Hz, with the strongest peak at 87.8 Hz (period of 11.4 ms). The higher-frequency region is markedly weaker than the lower-frequency region, extending from 160 to 187 Hz, with the strongest peak at 178.5 Hz (period of 5.6 ms). Once again, the higher frequency corresponds to the average eddy-shedding frequency, and the lower region represents the passing of vortices through the monitoring point.

As the Reynolds number was increased, the vortex-shedding frequency also increased, as did the rate at which vortices went past the monitoring point. The ratio of shedding frequency (in Hz) to Reynolds number was about constant, with a value of ~ 0.1 . Experimental²⁸ and numerical²⁹ works suggest that the Strouhal number for circular cylinders increases slightly with Reynolds number and stabilizes at ~ 0.21 for cylinder Reynolds numbers > 500 . Using $1.82 \times$ the inlet velocity as the reference velocity (which is, in fact, the average velocity of the fluid in the gap between the filament and the opposite wall) and the filament diameter as the length scale, we obtain Strouhal number values of 0.199 and 0.218 for the flows at hydraulic Reynolds numbers of 841 and 1683, respectively. The cylinder Reynolds numbers for these flows are 417 and 915, respectively, using the velocity of the fluid in the gap as the reference velocity, which represents a very good agreement (5.24% and 3.81% relative error) with the reported value. Moreover, the peak representing the shedding frequency in the power spectrum became weaker than the peak associated with the passing of eddies as the Reynolds number was increased. This corresponds with the appearance of larger eddies closer to the downstream spacer at the higher Reynolds number. It also suggests that the disturbances generated by the shedding of the vortices at the spacer filaments lose strength as they travel downstream.

4. Conclusions

For the zigzag geometry simulated in this work, it was observed that the flow becomes unsteady at a hydraulic Reynolds number between 526 and 841. It was found that the regions of higher mass transfer on the membrane wall are correlated not only to those of high shear rate but also to those where the fluid flow is toward the wall. Likewise, the wall regions in which the fluid flow is away from the wall correspond to those of low mass transfer. Knowledge of the location of the regions of low and high friction and mass transfer on the membrane surface is particularly important for spacer design. New filament profiles could be devised in an attempt to influence the fluid flow in order to increase wall shear rate in the regions where mass transfer is low, while retaining the current flow characteristics for the regions where it is already high. The exponents for the Reynolds number dependence of the Sherwood number for the empty channel and the channel with the zigzag spacer at steady state were 0.332 and 0.605, respectively. In unsteady flow, the exponent increased to 0.92 for the zigzag spacer because of the higher density of wall

vortices per channel unit length. Vortices near the membrane walls enhance mass transfer because of two main effects: an increased wall shear, which decreases the thickness of the boundary layer, and an inflow of lower-concentration fluid into the boundary layer. The results in this paper indicate that inflow of lower-concentration fluid into the boundary layer dominates unsteady mass-transfer enhancement for membrane filtration of sodium chloride.

For a constant Schmidt number, a thinner concentration boundary layer represents a higher degree of mass transfer. On the other hand, concentration boundary layer thickness is inversely proportional to Schmidt number. Therefore, for a higher Schmidt number (such as those encountered in UF and MF), the low-concentration fluid moved toward the channel walls by the passing vortices must come closer to the wall to retain the same degree of mass transfer. This means that, for higher Schmidt number solutes, the efficiency of scouring vortices is lower. To maintain a high mass-transfer coefficient at a high Schmidt number, mechanisms must be found to decrease the size of the velocity boundary layer, thus enabling velocity fluctuations to approach closer to the wall and disturb the concentration boundary layer.

Acknowledgment

The authors would like to acknowledge the Australian Research Council for funding this project through a Discovery grant. One of us (G.A.F.-W.) would also like to thank the University of New South Wales and the Faculty of Engineering for scholarship funding.

List of Symbols

Symbols

a, b, c, d = empirical constants in eq 3
 D = diffusion coefficient = m^2/s
 d_f = filament diameter = m
 d_h = hydraulic diameter = m
 F = vortex shedding frequency = Hz
 $f = (d_h/2\rho u_{\text{eff}}^2)(\Delta p/L)$ = Fanning friction factor
 $f_{\text{loc}} = (\tau_w/(1/2)\rho u_{\text{eff}}^2)$ = local friction factor
 h_{ch} = channel height = m
 h_f = filament height = m
 k_{mt} = mass-transfer coefficient = m/s
 L = channel length = m
 l_f = filament length = m
 l_m = mesh length = m
 p = pressure = Pa
 Re = Reynolds number
 $Re_{\text{ch}} = (\rho u_{\text{avg}} h_{\text{ch}}/\mu)$ = channel Reynolds number
 $Re_{\text{cyl}} = (\rho u_{\text{avg}} d_f/\mu)$ = cylinder Reynolds number
 $Re_h = (\rho u_{\text{eff}} d_h/\mu)$ = hydraulic Reynolds number
 $Sc = (\mu/\rho D)$ = Schmidt number
 $Sh = (k_{\text{mt}} d_h/D)$ = Sherwood number
 $Sh_{\text{loc}} = (d_h/(Y_w - Y_{\text{avg}}))(\partial Y/\partial y)_w$ = local Sherwood number
 $Sr = (F d_f/u)$ = Strouhal number
 t = time = s
 t_{st} = time step size = s
 u = velocity in x direction = m/s
 $u_{\text{eff}} = u_{\text{avg}}/\epsilon$ = effective velocity = m/s
 v = velocity in y direction = m/s
 x = distance in bulk flow direction = m
 Y = salt mass fraction
 y = distance in direction perpendicular to bulk flow = m

Greek Symbols

δ = boundary layer thickness = m

δ_{conc} = concentration boundary layer thickness = m

δ_{vel} = velocity boundary layer thickness = m

ϵ = void fraction, porosity

μ = dynamic viscosity of the fluid = (kg/m·s)

ρ = density of the fluid = kg/m³

τ_w = wall shear rate = Pa

Subscripts

avg = average value integrated over channel cross section

b = mass flow average or bulk flow value

w = value at the channel wall

Literature Cited

- (1) Sourirajan, S. *Reverse Osmosis*; Academic Press: New York, 1970.
- (2) Schwinge, J.; Wiley, D.; Fletcher, D. F. Simulation of Unsteady Flow and Vortex Shedding for Narrow Spacer-Filled Channels. *Ind. Eng. Chem. Res.* **2003**, *42*, 4962.
- (3) Zhou, W.; Song, L.; Guan, T. K. A numerical study on concentration polarization and system performance of spiral wound RO membrane modules. *J. Membr. Sci.* **2006**, *271*.
- (4) Schock, G.; Miquel, A. Mass transfer and pressure loss in spiral wound modules. *Desalination* **1987**, *64*, 339.
- (5) Kang, I. S.; Chang, H. N. The Effect of Turbulence Promoters on Mass Transfer—Numerical Analysis and Flow Visualization. *Int. J. Heat Mass Transfer* **1982**, *25*, 1167.
- (6) Da Costa, A. R.; Fane, A. G.; Wiley, D. E. Spacer characterization and pressure drop modelling in spacer-filled channels for ultrafiltration. *J. Membr. Sci.* **1994**, *87*, 79.
- (7) Ghidossi, R.; Veyret, D.; Moulin, P. Computational fluid dynamics applied to membranes: State of the art and opportunities. *Chem. Eng. Process* **2006**, *45*.
- (8) Schwinge, J.; Wiley, D.; Fletcher, D. F. Simulation of the Flow around Spacer Filaments between Channel Walls. 2. Mass-Transfer Enhancement. *Ind. Eng. Chem. Res.* **2002**, *41*, 4879.
- (9) Schwinge, J.; Wiley, D.; Fletcher, D. F. Simulation of the Flow around Spacer Filaments between Channel Walls. 1. Hydrodynamics. *Ind. Eng. Chem. Res.* **2002**, *41*, 2977.
- (10) Geraldes, V.; Semiao, V.; de Pinho, M. N. Flow and mass transfer modelling of nanofiltration. *J. Membr. Sci.* **2001**, *191*, 109.
- (11) Geraldes, V.; Semiao, V.; de Pinho, M. N. The effect on mass transfer of momentum and concentration boundary layers at the entrance region of a slit with a nanofiltration membrane wall. *Chem. Eng. Sci.* **2002**, *57*, 735.
- (12) Geraldes, V.; Semiao, V.; de Pinho, M. N. Flow management in nanofiltration spiral wound modules with ladder-type spacers. *J. Membr. Sci.* **2002**, *203*, 87.
- (13) Geraldes, V.; Semiao, V.; de Pinho, M. N. Concentration polarization and flow structure within nanofiltration spiral-wound modules with ladder-type spacers. *Comput. Struct.* **2004**, *82*, 1561.
- (14) Koutsou, C. P.; Yiantsios, S. G.; Karabelas, A. J. Numerical simulation of the flow in a plane-channel containing a periodic array of cylindrical turbulence promoters. *J. Membr. Sci.* **2004**, *231*, 81.
- (15) Subramani, A.; Kim, S.; Hoek, E. M. V. Pressure, flow, and concentration profiles in open and spacer-filled membrane channels. *J. Membr. Sci.* **2006**, *277*.
- (16) Karode, S. K.; Kumar, A. Flow visualization through spacer filled channels by computational fluid dynamics. I. Pressure drop and shear rate calculations for flat sheet geometry. *J. Membr. Sci.* **2001**, *193*, 69.
- (17) Ranade, V. V.; Kumar, A. Fluid dynamics of spacer filled rectangular and curvilinear channels. *J. Membr. Sci.* **2006**, *271*.
- (18) Li, F.; Meindersma, W.; de Haan, A. B.; Reith, T. Optimization of commercial net spacers in spiral wound membranes modules. *J. Membr. Sci.* **2002**, *208*, 289.
- (19) Gimmelshtein, M.; Semiat, R. Investigation of flow next to membrane walls. *J. Membr. Sci.* **2005**, *264*.
- (20) Bird, R. B.; Stewart, W. E.; Lightfoot, E. N. *Transport Phenomena*; Wiley: New York, 1960.
- (21) Wiley, D.; Fletcher, D. F. Techniques for computational fluid dynamics modelling of flow in membrane channels. *J. Membr. Sci.* **2003**, *211*, 127.
- (22) Fletcher, D. F.; Wiley, D. A computational fluids dynamics study of buoyancy effects in reverse osmosis. *J. Membr. Sci.* **2004**, *245*, 175.
- (23) Versteeg, H. K.; Malalasekera, W. *An Introduction to Computational Fluid Dynamics: The Finite Volume Method*; Prentice Hall: London, 1995.
- (24) Rhie, C. M.; Chow, W. L. *A Numerical Study of the Turbulent Flow Past an Isolated Airfoil with Trailing Edge Separation*; AIAA Paper 82-0998; American Institute of Aeronautics and Astronautics: Reston, VA, 1982.
- (25) Rosén, C.; Trägårdh, C. Computer Simulations of mass transfer in the concentration boundary layer over ultrafiltration membranes. *J. Membr. Sci.* **1993**, *85*, 139.
- (26) Treybal, R. E. *Mass-transfer operations*; McGraw-Hill: New York, 1980.
- (27) Da Costa, A. R. Fluid Flow and Mass Transfer in Spacer-Filled Channels for Ultrafiltration. Ph.D. Thesis, The University of New South Wales, Sydney, Australia, 1993.
- (28) Williamson, C. H. K. Defining a universal and continuous Strouhal—Reynolds number relationship for the laminar vortex shedding of a circular cylinder. *Phys. Fluids* **1988**, *31*.
- (29) Ozgoren, M. Flow structure in the downstream of square and circular cylinders. *Flow Meas. Instrum.* **2006**, *17*.

Received for review February 26, 2006
 Revised manuscript received June 19, 2006
 Accepted July 13, 2006

IE060243L